

Cite this: *Energy Adv.*, 2022,
1, 877

Lithium recovery from geothermal brine – an investigation into the desorption of lithium ions using manganese oxide adsorbents

Laura Herrmann,^{id}*^{ab} Helmut Ehrenberg,^{id}^b Magdalena Graczyk-Zajac,^a
Elif Kaymakci,^a Thomas Kölbel,^a Lena Kölbel^c and Jens Tübke^d

Spinel type lithium manganese oxides (LMOs) are promising adsorption materials for selective recovery of lithium from salty brines. In this work a lithium-ion sieve material, $H_{1.6}Mn_{1.6}O_4$, derived from $Li_{1.6}Mn_{1.6}O_4$, a spinel type LMO, was successfully prepared via hydrothermal synthesis. This lithium-ion sieve, $H_{1.6}Mn_{1.6}O_4$, was then used in laboratory tests to adsorb Li^+ from a generic LiCl solution and geothermal brine from Bruchsal geothermal power plant. Desorption experiments were performed with the following desorption solutions: ammonium peroxydisulfate ($(NH_4)_2S_2O_8$), sodium peroxydisulfate ($Na_2S_2O_8$), acetic acid (CH_3COOH), sulfuric acid (H_2SO_4), carbonic acid (H_2CO_3), ascorbic ($C_6H_8O_6$) and hydrochloric acid (HCl). The results showed that $C_6H_8O_6$ led to adsorbent destruction and only small amount of lithium was desorbed with H_2CO_3 . CH_3COOH and $(NH_4)_2S_2O_8$ showed the best desorption performance with high lithium recovery and low Mn dissolution. The kinetic experiments indicate that more than 90% of equilibrium was reached after 4 hours. A decline in the adsorption/desorption capacity was measured for all desorption agents after eight cycles in the long-term experiments. These long-term tests revealed that higher lithium recovery in desorption with HCl and CH_3COOH was achieved compared to $(NH_4)_2S_2O_8$. On the other hand, the use of CH_3COOH and $(NH_4)_2S_2O_8$ seems to be advantageous to HCl because of lower Mn dissolution. According to the XRD results, the spinel structure of the treated adsorbents was preserved, but a weakening of the peak intensity was observed. Analyzing the adsorbent composition after eight cycles, an accumulation of competing ions was observed. This was especially remarkable when acetic acid was used.

Received 29th April 2022,
Accepted 12th September 2022

DOI: 10.1039/d2ya00099g

rsc.li/energy-advances

1. Introduction

Geothermal energy is a renewable energy resource offering both, power production as well as direct heat supply on a temperature level sufficient for industrial processes and district heating with a very high system availability. Its contribution to the world's energy consumption amounted to 630 petajoules in 2018, equally shared by electricity and heat.¹ Taking the high availability of geothermal plants (>90%) and an average mass flow of a geothermal doublet of 30–80 l s⁻¹ into account, a remarkable volume of hot fluids is produced and reinjected per year. The total dissolved solid content of geothermal brines ranges from single to some hundreds of grams per liter.

Depending on their geological origin geothermal brines contain several raw materials including lithium (Li) with concentrations between 0.1 and 500 mg l⁻¹.^{2,3} The forthcoming global energy transition requires a shift to new and renewable technologies, which increase the demand for related materials, especially lithium. Due to its function in a lithium-ion battery, it takes on a fundamental role in fully renewable energy systems.⁴ In recent years the global demand for lithium has rapidly increased and it is anticipated to increase from around 270 Kt LCE in 2019 to over 2600 Kt LCE by 2030. Therefore, the extraction of raw material from non-conventional sources and alternative extraction methods are recently in the focus of academic and industrial research.⁵ The extraction of lithium from geothermal brine offers a great opportunity for regional supply chains. In Germany, high lithium concentrations are measured in hot geothermal brines in the North German Basin (NDB) (up to 240 mg l⁻¹) and in the Upper Rhine Valley (100–200 mg l⁻¹).^{6,7} In these regions, several geothermal plants are already in operation. At a geothermal power plant, geothermal brine is pumped to the earth's surface and its thermal energy is used to generate heat

^a EnBW Energie Baden-Württemberg AG, Durlacher Allee 93, 76131 Karlsruhe, Germany. E-mail: lherrmann@enbw.com

^b Karlsruher Institut für Technologie (KIT) – Institut für Angewandte Materialien (IAM), Hermann-von-Helmholtz-Platz 1, 76344 Eggenstein-Leopoldshafen, Germany

^c Hydrosion GmbH, Tizianstr. 96, 80638 Munich, Germany

^d Fraunhofer Institute for Chemical Technology (ICT), Joseph-von-Fraunhofer-Str. 7, 76327 Pfinztal, Germany



and electricity. Subsequently, the geothermal brine is reinjected into the subsurface.⁸ Successful recovery of raw materials from geothermal brines as co-product besides electricity and heat supply will lead to additional economic benefits and increase the potential of exploiting deep geothermal energy, thus, contribute to sustainable energy production and regional lithium extraction.

In addition to extracting lithium from geothermal brines, there are also reports on extracting the metal *via* non-conventional methods from other lithium water resources such as salt lake brines which also have high Li concentrations *e.g.* 266 mg l⁻¹ and seawater,⁹ which has rather low Li concentrations *e.g.* 0.17 mg l⁻¹,¹⁰ but is available in large amounts. Among numerous extraction technologies, adsorption is considered as one of the most promising recovery technologies. Recovery of lithium from geothermal brine is particularly challenging due to the large number of competing ions.¹¹ Due to their high adsorption capacity and high selectivity, lithium manganese oxides (LMOs) are the most promising materials for Li⁺ recovery from aqueous solutions.¹⁰ The ion sieve H_{1.6}Mn_{1.6}O₄ with a high theoretical lithium adsorption capacity of 68 mg g⁻¹ is considered as a promising adsorbent candidate.⁹ Chitrakar *et al.* (2001) also measured high adsorption lithium capacities using the ion sieve H_{1.6}Mn_{1.6}O₄.¹⁰ LMOs show ion sieve properties. They have spinel structure with pore radii which, due to their size, only allow Li⁺ ions and H⁺ ions to pass and can therefore be used selectively for Li extraction. Shi *et al.* (2011) showed that the adsorbent exhibited high selectivity toward Mg, Na, and K in an environment dominated by competing ions.⁹ However, the desorption process using HCl was accompanied by a high dissolution of Mn. This limits industrial application due to a loss of active adsorbent component in each regeneration step. Thus, the chemical stability of the adsorbent represents an important criterion, necessary to ensure a sufficient economic performance in industrial applications.¹¹ In this study, lithium extraction from geothermal brine of the Bruchsal geothermal plant using LMO-derived adsorbent H_{1.6}Mn_{1.6}O₄ was investigated. Various desorption agents ((NH₄)₂S₂O₈, Na₂S₂O₈, CH₃COOH, H₂SO₄, H₂CO₃, C₆H₈O₆ and HCl) were tested for their ability to desorb lithium from the loaded sorbent Li_{1.6}Mn_{1.6}O₄. In particular, the impact of the eluent solution on desorption capacity, desorption kinetic, chemical neutrality with respect to the sorbent and the sustainability was addressed. The performance of various desorption agents was investigated in desorption experiments and their technical suitability considering various parameters was evaluated.

1.1 Geothermal fluid chemistry

It is well known that the deep geothermal brines in the Upper Rhine Valley are enriched with lithium.^{12,13} Sanjuan *et al.* (2016) reported lithium concentrations as high as 200 mg l⁻¹ and δ⁷Li lithium isotope signatures between 1.0 and 1.7‰.⁷

At Bruchsal, the lithium content in the geothermal brine is about 150 mg l⁻¹ (*cf.*, Table 1). The produced brine (of the Na–Ca–Cl type) is highly concentrated in chloride, sodium and other alkali metals and alkaline earth metals, containing up to 130 g l⁻¹ of total dissolved solids (TDS). Furthermore, the brine

Table 1 Components of the geothermal brine Bruchsal

| K [mg l ⁻¹] | Na [mg l ⁻¹] | Ca [mg l ⁻¹] | Mg [mg l ⁻¹] | Sr [mg l ⁻¹] |
|--------------------------|--------------------------|--------------------------|--------------------------|--------------------------|
| 3538 | 41 327 | 9194 | 415 | 374 |
| Fe [mg l ⁻¹] | Ba [mg l ⁻¹] | Pb [mg l ⁻¹] | Al [mg l ⁻¹] | Li [mg l ⁻¹] |
| 50.3 | 8.9 | 3.2 | 2.2 | 141 |

is enriched in sulfate (339 mg l⁻¹) and hydrogen carbonate (341 mg l⁻¹) as well as heavy metals such as lead, arsenic, and cadmium. In contrast, the concentration of organic compounds is low. The pH conditions are difficult to determine because of the change in pressure and temperature between reservoir and the sampling location at ground level. At the sampling point, pH value is 5.5. Under standard conditions, the ratio of the aqueous phase to the gas phase is 1:1.6 whereby carbon dioxide represents the main gas component (approximately 90 vol% of the total gas phase).¹⁴

2. Experiments

2.1 Preparation of material

The method of synthesizing the adsorbent was based on the experiments of Chitrakar *et al.* (2001) and Shi *et al.* (2011).^{9,10} First, 70 g of MnO₂ (Manufacturer purity: 99.997%) was calcined at 680 °C in an oven for 6 hours to obtain Mn₂O₃. A total of 5 g Mn₂O₃ were mixed with 100 ml of a 4 M LiOH solution in a stainless-steel vessel (125 ml) with a Teflon-inlet. The mixture was autoclaved for 24 hours at 120 °C to obtain orthorhombic LiMnO₂ *via* hydrothermal synthesis. Subsequently the LiMnO₂ was calcined at 400 °C for 4 hours in air to obtain the lithium ion-sieve precursor Li_{1.6}Mn_{1.6}O₄. The suspension was filtered, washed with deionized water, and dried for 24 hours at 60 °C. The procedure was applied to produce a total of three batches.

2.2 Physical analysis

Powder X-ray diffraction (XRD) (STOE Stadi P; STOE & Cie GmbH) of the materials was obtained using Mo-Kα-radiation (λ = 0.0790 nm) at 50 kV, 40 mA, 0.0055° s⁻¹ scanning speed, and a range from 6° to 50°. Scanning electron microscopy (SEM) was conducted to visualize the surface morphology of the raw and treated adsorbent using a SEM of type MERLIN (Zeiss).

2.3 Chemical analysis

The ion concentrations of Li, Mn and competing ions were analyzed by inductively coupled plasma optical emission spectroscopy (ICP-OES). The adsorbent was dissolved in a 37 wt% HCl solution and then diluted. Finally, the composition of the adsorbent was determined using ICP-OES (700 Series: Agilent Technologies). Single determinations are given as single values, multiple determinations as mean values of the multiple determinations including standard deviation. The errors were rounded to one significant digit. The last significant digit of the measured value is in the same order of magnitude as the measurement uncertainty.



2.4 Adsorption/desorption of lithium

Table 2 provides an overview of different experiments. Adsorption and desorption processes are based on ion exchange mechanism, as described in eqn (1).



For the preliminary tests, 5 g of the adsorbent (batch 1) were mixed with 2.270 ml of LiCl solution ($c_{\text{Li}^+} = 150 \text{ mg l}^{-1}$) with a pH of 7.9 ± 0.1 . The suspension was stirred at $25 \text{ }^\circ\text{C}$ for 24 hours. For the kinetics tests 7.7 g of the adsorbent (batch 1) were mixed with 3495.8 ml of geothermal brine ($c_{\text{Li}^+} = 142 \text{ mg l}^{-1}$) with a pH of 5.5 ± 0.1 . The suspension was stirred at $25 \text{ }^\circ\text{C}$ for 24 hours. For each long-term cycling experiment 220 mg of adsorbent (batch 2) were mixed with 100 ml of geothermal brine ($c_{\text{Li}^+} = 142 \text{ mg l}^{-1}$) with a pH of 6.6 ± 0.1 . The suspension was stirred at $60 \text{ }^\circ\text{C}$ for 4 hours. The concentration of Li^+ in the solution was measured by ICP-OES. The adsorption capacity Q was calculated according to eqn (2)

$$Q = (c_0 - c) V/m_s \quad (2)$$

where V were the volume of the solution and m_s the mass of the adsorbent. c_0 is the initial concentration and c the concentration at time t .⁹

The Li solutions used for loading the adsorbents are listed in Table 2 for each experiment. For desorption tests the Li-loaded adsorbents ($\text{Li}_{1.6}\text{Mn}_{1.6}\text{O}_4$) were mixed with different desorption agents to desorb lithium. For the preliminary tests 20 ml of desorption agent was mixed with 0.3 g of Li-loaded adsorbent and the solution was stirred for 24 hours. The desorption tests were conducted at $25 \text{ }^\circ\text{C}$ and $60 \text{ }^\circ\text{C}$. Aqueous solutions of 0.5 M HCl, CH_3COOH , H_2SO_4 , $(\text{NH}_4)_2\text{S}_2\text{O}_8$, $\text{Na}_2\text{S}_2\text{O}_8$, $\text{C}_6\text{H}_8\text{O}_6$ and 5 mmol l^{-1} H_2CO_3 , were tested as desorption agents. The desorption agent with the best performance (CH_3COOH , $(\text{NH}_4)_2\text{S}_2\text{O}_8$) regarding Li^+ -recovery and Mn dissolution rates were selected for further tests and their results were compared with those of HCl as a reference. For each batch of the kinetics tests, a mixture of 0.18 g of the Li-loaded adsorbent and 12 ml of desorption agent ($60 \text{ }^\circ\text{C}$) were stirred for 30 s, 60 s, 2 min, 30 min, 4 hours, and 24 hours. The temperature was kept constant at $60 \text{ }^\circ\text{C}$. In long term cycling experiments, a mixture of 220 mg of the Li-loaded adsorbent and 14.67 ml of desorption agent ($60 \text{ }^\circ\text{C}$) per batch were stirred for 4 hours. The long-term experiments were carried out for eight cycles. The Li^+ concentration after desorption reaction was determined by ICP-OES. The Li^+ recovery rate R was calculated from the ratio of desorbed Li^+ ($m_{\text{Li,des}}$) to the total amount of Li in the

adsorbent after adsorption step ($m_{\text{Li,ads}}$) as indicated in eqn (3).

$$R = \frac{m_{\text{Li,des}}}{m_{\text{Li,ads}}} \quad (3)$$

2.5 Modeling

To describe the reaction kinetics, the pseudo-first order kinetic model, which is shown in eqn (4) and (5) was used and related to the results of the kinetic experiments.¹⁵

$$\ln(Q_{d,\text{eq}} - Q_d) = \ln(Q_{d,\text{eq}}) - K_1 t \quad (4)$$

$$Q_d(t) = Q_{d,\text{eq}} (1 - e^{-K_1 t}) \quad (5)$$

where Q_d is the desorption capacity at time t . The desorption capacity at equilibrium is $Q_{d,\text{eq}}$ and K_1 is the reaction constant. The curve fit algorithm of the Python library SciPy. Optimize was used, which is based on the non-linear least square's method.

3. Results

3.1 Preparation of $\text{H}_{1.6}\text{Mn}_{1.6}\text{O}_4$

Fig. 2 shows the XRD patterns of the synthesized and then four times washed adsorbent $\text{H}_{1.6}\text{Mn}_{1.6}\text{O}_4$. The diffraction patterns of the samples match well with the cubic spinel structure of the $\text{Li}_{1.6}\text{Mn}_{1.6}\text{O}_4$ reference pattern (ICDD 00-052-1841) with a $Fd\bar{3}m$ space group. All characteristic reflections of the spinel are present, however, the results show an unassigned peak for the adsorbent at 25.1° .

3.2 Adsorption/desorption performance

The results of the adsorption/desorption experiments are illustrated in Fig. 1. In Fig. 1a the Li^+ recovery using various desorption agents is presented. The highest Li^+ recovery of more than 97% is obtained with HCl, H_2SO_4 and CH_3COOH at $60 \text{ }^\circ\text{C}$. The lowest Li^+ recovery of 5.4% ($60 \text{ }^\circ\text{C}$) and 7.4% ($25 \text{ }^\circ\text{C}$) is found with H_2CO_3 . Among the persulfates, $(\text{NH}_4)_2\text{S}_2\text{O}_8$ shows a higher desorption performance compared to that of $\text{Na}_2\text{S}_2\text{O}_8$ with a Li^+ -recovery of 71.9% ($60 \text{ }^\circ\text{C}$) and 59.7% ($25 \text{ }^\circ\text{C}$). In general, a higher temperature is found to be advantageous for the efficiency of the desorption step.

Fig. 1b shows the Mn dissolution in the desorption step when various desorption agents are used. HCl and H_2SO_4 lead to the highest Mn dissolution of 367.4 mg l^{-1} ($60 \text{ }^\circ\text{C}$) and 138.3 mg l^{-1} ($60 \text{ }^\circ\text{C}$), respectively. On the other hand, CH_3COOH , H_2CO_3 and persulfates result in a significantly lower Mn release. The results of the ICP-OES analysis show that $\text{C}_6\text{H}_8\text{O}_6$ leads to an almost complete dissolution of the adsorbent, since more than 90% of the Mn is measured in the supernatant.

Table 2 Comparison of the different adsorption/desorption experiments. Li^+ -solution, pH value and temperature were varied

| Experiment | Adsorption | | | | Desorption | |
|-------------------|------------|-------------------------|---------------|----------------------------------|--|----------------------------------|
| | Batch | Li^+ -solution | pH | Temperature ($^\circ\text{C}$) | Q_{ad} (mg g^{-1}) | Temperature ($^\circ\text{C}$) |
| Preliminary | 1 | LiCl | 7.9 ± 0.1 | 25 | 6.22 | 25, 60 |
| Kinetics | 1 | Geothermal brine | 5.5 ± 0.1 | 25 | 2.64 | 60 |
| Long-term cycling | 2 | Geothermal brine | 6.6 ± 0.1 | 60 | — | 60 |



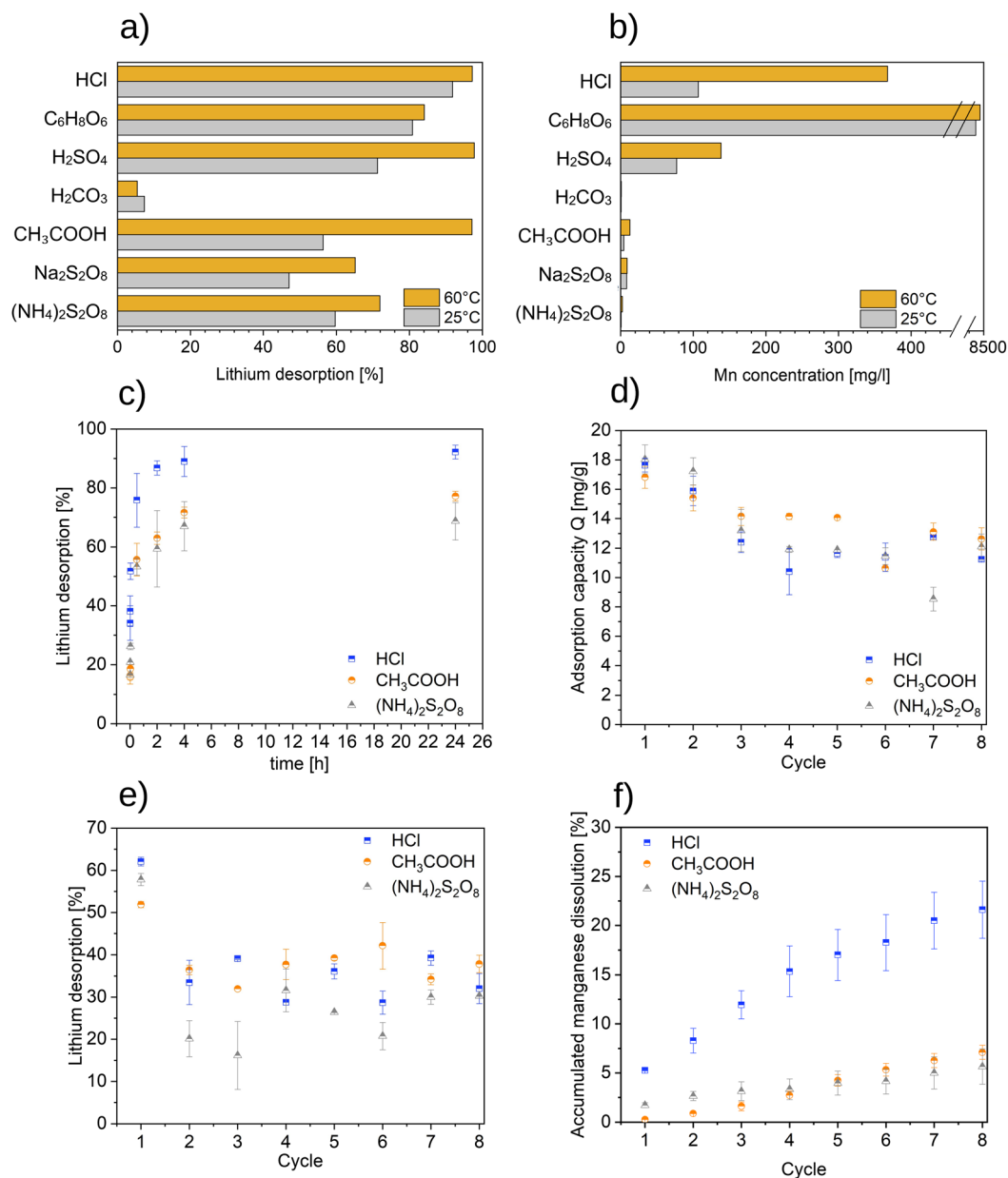


Fig. 1 (a) ICP-OES Data of the Li recovery in preliminary desorption test using several desorption agents at 25 °C and 60 °C. (b) Mn dissolution in the preliminary tests using different desorption agents at 25 °C and 60 °C. (c) Li recovery over time using different desorption agents. (d) Cycle performance of adsorptions step using geothermal brine at 60 °C. (e) Cycle performance of Li recovery using various desorption agents at 60 °C. (f) Accumulated Mn dissolution over eight cycles.

Fig. 1c shows the results of the kinetics experiment using various desorption agents in the desorption step. In the first minutes, a high reaction rate is observed for all tested desorption agents. The highest Li⁺ recovery rate amounts $92.19 \pm 2.3\%$ and is achieved after 24 hours using the desorption agent HCl. The figure shows too that 90% of the equilibrium concentration is reached after 4 hours for all tested desorption agents.

In Fig. 1d the adsorption capacity of the long-term experiments over eight cycles is presented. The maximum adsorption capacity is recorded for all desorption agents in the first cycle, it drops and starting from the third cycle it remains almost constant. After eight cycles, the adsorption capacity of the

adsorbent is $11.3 \pm 0.1 \text{ mg g}^{-1}$ when using HCl, $12.6 \pm 0.8 \text{ mg g}^{-1}$ when using CH₃COOH and $12.1 \pm 0.9 \text{ mg g}^{-1}$ when using (NH₄)₂S₂O₈. The desorption capacity over eight cycles using various desorption agents is given in Fig. 1e. The maximum desorption capacity for all desorption agents is found in the first cycle followed by a significant decrease in following cycles. Li⁺ recovery rate levels off at 30–40% in the use of HCl and CH₃COOH, while it is somewhat lower in the use of (NH₄)₂S₂O₈. After eight cycles the Li⁺ recovery rate amounts to $32.0 \pm 3.6\%$ using HCl, $37.8 \pm 0.3\%$ using CH₃COOH and $30.3 \pm 0.0\%$ using (NH₄)₂S₂O₈.

In Fig. 1f the Mn dissolution over eight cycles using various desorption agents is presented. After the first HCl desorption



cycle $5.3 \pm 0.1\%$ of Mn is dissolved. Whereas when using CH_3COOH and $(\text{NH}_4)_2\text{S}_2\text{O}_8$ the Mn dissolution is significantly lower, $0.3 \pm 0.0\%$ and $1.7 \pm 0.3\%$, respectively. After eight HCl desorption cycles, $21.6 \pm 2.9\%$ of the Mn is dissolved while only $7.1 \pm 0.7\%$ and $5.6 \pm 1.8\%$ of Mn is dissolved in 8 cycles with CH_3COOH and $(\text{NH}_4)_2\text{S}_2\text{O}_8$, respectively.

3.3 Material characterization

Fig. 2a shows the XRD patterns of the raw adsorbent as well as the adsorbent used in long-term experiments for eight cycles. The resulting diffraction pattern of the raw adsorbent is consistent with the diffraction data for the corresponding phases published in the ICDD database.¹⁰ For all the tested desorption agents, the spinel reflections are preserved, but some structural inconsistencies are identified. Desorption of Li^+ ions with CH_3COOH leads to a significant reduction of the intensity of reflections of $\text{H}_{1.6}\text{Mn}_{1.6}\text{O}_4$. After desorption with HCl, the diffraction pattern of the adsorbent remains the most this of the pristine material. When $(\text{NH}_4)_2\text{S}_2\text{O}_8$ is used, new reflections appear between 10° and 15° .

The SEM micrographs of the raw adsorbent and the adsorbents treated with HCl, $(\text{NH}_4)_2\text{S}_2\text{O}_8$ and CH_3COOH after eight cycles are shown in Fig. 2c–f. The image in Fig. 2c reveals heterogeneous, densely packed agglomerates. These are composed of partly plate-shaped, but mainly small, cubic particles. The individual grains are mostly $<0.1 \mu\text{m}$. The adsorbent regenerated with HCl (Fig. 2d) shows great similarity to the raw adsorbent. The adsorbent regenerated with $(\text{NH}_4)_2\text{S}_2\text{O}_8$ (Fig. 2e) has both plates and cuboids structures. The particle size distribution is clearly wider and more plates with diameters larger than $>0.1 \mu\text{m}$ are visible. The image of the adsorbent treated with CH_3COOH (Fig. 2e) shows nodular

structures and a wide particle size distribution. After eight cycles, clear changes in all adsorbent structures are found.

Fig. 2b shows the accumulation of the competing ions in the lithium-ion sieve. The measured values listed in Table 3 result from ICP-OES analyses of the adsorbents decomposed using 37% HCl. In general, an accumulation of competing ions in the ion sieve is found in all samples. However, this phenomenon is particularly striking for the desorption agent CH_3COOH , which leads to a significant accumulation of lead (Pb), barium (Ba), calcium (Ca), sodium (Na), potassium (K), magnesium (Mg), and iron (Fe) on the adsorbent. Hereby, the concentrations of lead and iron are the highest at 18.9 mg g^{-1} and 23.5 mg g^{-1} . Solely the accumulation of sodium and aluminum is more pronounced in the adsorbent treated with HCl ($\text{Na} = 15.0 \text{ mg g}^{-1}$, $\text{Al} = 1.2 \text{ mg g}^{-1}$). The adsorbent treated with $(\text{NH}_4)_2\text{S}_2\text{O}_8$ generally presents a low enrichment with competing ions. Here, iron forms the largest fraction with 6.15 mg g^{-1} .

4. Discussion

4.1 Adsorption performance

In the preliminary tests, an adsorption capacity of 6.22 mg g^{-1} was obtained using 150 mg l^{-1} LiCl solution at a pH of 7.86. This result shows a similar tendency to the results of the study from Shi *et al.*, in which a slightly lower adsorption capacity of 4.16 mg g^{-1} using synthetic brine at a pH of 7.85 was reported.¹⁶ In the long-term cycling experiments geothermal brine with pH of 6,6 was used. After the first cycle, an adsorption capacity between $(16.8 \pm 0.8) \text{ mg g}^{-1}$ and $(18.0 \pm 1.0) \text{ mg g}^{-1}$ was achieved, which was significantly higher than that in the preliminary experiments ($Q = 6.2 \text{ mg g}^{-1}$) and that in the kinetics

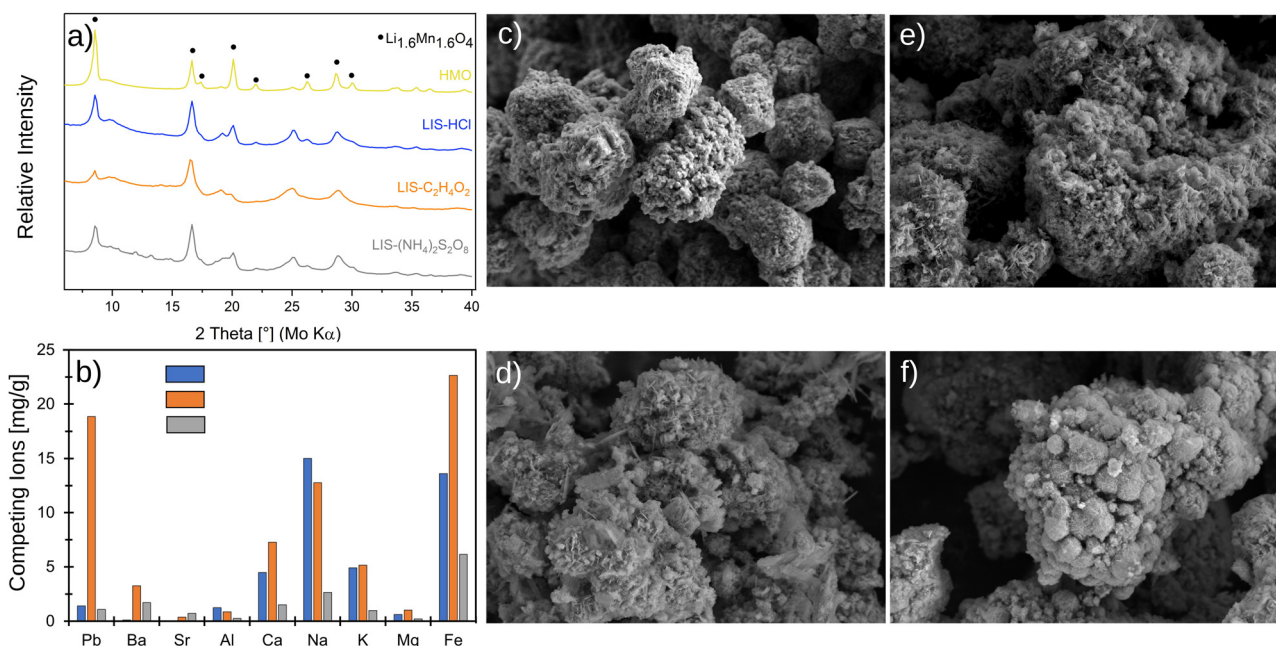


Fig. 2 (a) X-ray diffraction patterns of Mn-oxides, HMO indicates the raw adsorbent, LIS is the lithium-ion-Sieve treated with various desorption agents over eight cycles. (b) Accumulation of various cations originating from geothermal brine. SEM images of (c) raw adsorbent ($\text{H}_{1.6}\text{Mn}_{1.6}\text{O}_4$) and with HCl (d), $(\text{NH}_4)_2\text{S}_2\text{O}_8$ (e) and CH_3COOH (f) treated adsorbent after eight cycles.



Table 3 Concentrations of competing ions in milligrams per gram of adsorbent (mg g^{-1}). Adsorbents are treated with hydrochloric acid (HCl), acetic acid (CH_3COOH) and ammonium peroxydisulfate ($(\text{NH}_4)_2\text{S}_2\text{O}_8$)

| | Pb | Ba | Sr | Al | Ca | Na | K | Mg | Fe |
|---------------------------------------|------|-----|-----|-----|-----|------|-----|-----|------|
| HCl | 1.4 | 0.1 | 0.1 | 1.2 | 4.5 | 15.0 | 4.9 | 0.6 | 13.6 |
| CH_3COOH | 18.9 | 3.3 | 0.4 | 0.9 | 7.3 | 12.8 | 5.1 | 1.0 | 23.5 |
| $(\text{NH}_4)_2\text{S}_2\text{O}_8$ | 1.1 | 1.7 | 0.7 | 0.3 | 1.5 | 2.7 | 1.0 | 0.2 | 6.1 |

experiment ($Q = 2.6 \text{ mg g}^{-1}$). The reason behind achieving higher adsorption capacity is likely to be related to temperature. While adsorption was carried out at 25°C in the preliminary tests and kinetics experiments, the long-term experiments was performed at 60°C . Furthermore, an increase in pH was observed while heating the geothermal brine, which affected the adsorption performance positively. According to Le Chatelier's principle,¹⁷ low concentrations of hydrogen ions shift the equilibrium of the ion exchange reaction to the right (*cf.* Eqn (1)), which enhances the efficiency of the adsorption process. The increase of the pH value was due to the degassing of CO_2 during stirring and heating of the geothermal brine. The adsorption capacities in the cyclic experiments are all in all slightly lower than those in Shi *et al.* They achieved an adsorption capacity of 22 mg g^{-1} using Salt brine at a pH of 5.3. On the one hand, this may have been due to the Li concentration of 270 mg l^{-1} in the salt brine, which is significantly higher than the Li concentration of 145 mg l^{-1} in the geothermal brine. Furthermore, Shi *et al.* reported only small pH changes in the adsorption step thanks to the complex composition of the salt brine which increases adsorption performance. This buffer effect is difficult to maintain in the geothermal brine.¹⁶

4.2 Desorption agents

The results of the preliminary tests showed that Li^+ desorption from $\text{Li}_{1.6}\text{Mn}_{1.6}\text{O}_4$ was possible with all tested desorption agents except ascorbic acid. The highest Li^+ recovery of more than 97% was obtained at 60°C when HCl, H_2SO_4 and CH_3COOH were used. However, high Mn dissolution at both 25°C and 60°C was observed with the use of HCl and H_2SO_4 , compared to that with the use of other desorption agents. Mn dissolution is an irreversible process in which Mn is released that was previously chemically bound to the adsorbent. This means a loss of active component and could lead to a collapse of the adsorbent structure if a relevant amount of Mn is released.¹⁶ The stability of the adsorbent is an important criterion for technical applications, to be able to use it over several adsorption and desorption cycles.¹¹ The production of adsorbent is an important cost factor of the extraction process and therefore has a great impact on the economic efficiency of the process.

Promising results in terms of Li^+ recovery and Mn dissolution were obtained when CH_3COOH was used. At 60°C , an almost complete recovery of Li^+ as well as a significantly reduced Mn release were observed in comparison with the use of HCl. The use of $\text{C}_6\text{H}_8\text{O}_6$ led to destruction of the adsorbent. Since this acid dissolves the adsorbent, it is rather unsuitable as a desorption agent. Therefore and because of its low environmental hazard

properties, it is more favorable to use $\text{C}_6\text{H}_8\text{O}_6$ for other purposes. Accidental release of the adsorbent during operation of the plant can lead to a clogging of the injection well. In this case, $\text{C}_6\text{H}_8\text{O}_6$ could be used to dissolve the adsorbent in the wellbore without causing damage, as well as in the filter room and surrounding reservoir. Especially on the reservoir performance itself, $\text{C}_6\text{H}_8\text{O}_6$ has a positive influence anyway. Therefore, in practice, it is often used in chemical stimulation of wells.¹⁸ When H_2CO_3 was used as the desorption agent, the Mn release approached to zero, but also the obtained Li^+ recovery was low. Only a low concentration of H_2CO_3 solution was possible to be prepared with the available apparatus, in which CO_2 was dissolved at the atmospheric pressure and ambient temperature. However, CO_2 is available in the Bruchsal geothermal plant at higher pressure, at which more CO_2 can be dissolved according to Henry's law.¹⁹ Using CO_2 at a higher concentration will possibly bring different results in terms of Li^+ recovery. Among persulfates, $(\text{NH}_4)_2\text{S}_2\text{O}_8$ was advantageous over $\text{Na}_2\text{S}_2\text{O}_8$ with a recovery of 71.9% at 60°C and only little Mn dissolution.

4.3 Kinetics

The kinetic model of pseudo-first order was used to fit the data of the kinetics experiment. Although the first two values of the desorption capacity of the $(\text{NH}_4)_2\text{S}_2\text{O}_8$ had very small uncertainties of the ordinate, they strongly deflected the model and did not fit the overall curve. It is suspected that these measured data contain errors in the time specification due to a short measurement duration, which was not possible to be estimated. For this reason, the desorption capacity values at $t_1 = 30 \text{ s}$ and $t_2 = 1 \text{ min}$ of $(\text{NH}_4)_2\text{S}_2\text{O}_8$ were disregarded in the parameter estimation. Table 4 shows the modelling results for the parameters $Q_{d,\text{eq}}$ and K_1 .

The results of the desorption tests showed that the reaction rate was high in the first minutes for all desorption agents. A desorption agent that has a desorption rate as effective as adsorption reduces the capital costs of the extraction process. This is because, a desorption agent with higher reaction kinetics requires a comparatively smaller reactor for the same lithium production rate. The fitted curve of the Li^+ desorption kinetics is shown in Fig. 3.

After four hours, more than 90% of equilibrium was reached with all desorption agents based on the measured values. Considering pseudo-first-order kinetic model, equilibrium was reached after less than one hour.

4.4 Cycle performance

In the cyclic tests, a lower lithium desorption was observed compared to the preliminary tests and kinetics experiments.

Table 4 Fitting of the function $Q_d(t)$ to the values of the desorption capacity. The parameters $Q_{d,\text{eq}}$ and K_1 and their standard deviation are given

| | $Q_{d,\text{eq}} [\text{mg g}^{-1}]$ | $K_1 [\text{h}^{-1}]$ |
|---------------------------------------|--------------------------------------|-----------------------|
| $(\text{NH}_4)_2\text{S}_2\text{O}_8$ | 3.4 ± 0.2 | 18.5 ± 2.3 |
| CH_3COOH | 4.2 ± 0.3 | 12.8 ± 2.2 |
| HCl | 5.3 ± 0.2 | 28.7 ± 3.9 |



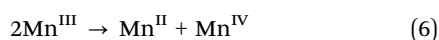


Fig. 3 Li desorption kinetics of different desorption agents and pseudo-first-order kinetic modeling.

The reasons for the lower lithium desorption are attributed to the fact that significantly more lithium was adsorbed in the cycling tests than in the kinetics and preliminary tests. For this high Li adsorption, the amount of desorption agent in the desorption step was not sufficient and must be further optimized. To make the process suitable for industrial application, the lithium must be desorbed to a high degree.

With the use of CH_3COOH and HCl similar Li^+ recovery over the eight cycles was observed, while slightly less lithium was desorbed when $(\text{NH}_4)_2\text{S}_2\text{O}_8$ was used in the cycle 2, 3 and 5–8. HCl is a strong acid which show a higher H^+ -content compared to weak acids at the same concentration. According to Le Chatelier's principle this favors the desorption step.¹⁷ The H^+ -concentration decreases during the desorption process, leading to an increase in pH value. However, the effect of the pH increase was less significant when the CH_3COOH solution was used because it forms a buffer system with Li^+ ions.

In the use of all desorption agents, manganese dissolutions were observed during the desorption step. In addition to the ion exchange reaction of Li^+ and H^+ ions, other reactions take place in the desorption step, in which the Mn^{III} is converted into Mn^{II} and Mn^{IV} by disproportionation effects (eqn (6)).



The bivalent manganese (Mn^{II}) is dissolved, while the tetravalent manganese (Mn^{IV}) remains in the ion sieve.²⁰ In addition to a loss of active component due to the release of bivalent Mn, an increase in Mn valence in the $\text{Li}_x(\text{Mn}_y^{\text{III}}\text{Mn}_z^{\text{IV}})\text{O}_4$ framework is expected in the cycling experiments. The change in the oxidation state of Mn is determined by X-ray photoelectron spectroscopy measurements and has been published in previous papers.²⁰

Using hydrochloric acid, Mn dissolution between 1% and 5% per cycle was measured. These values are consistent with the Mn dissolution in Chitrakar *et al.* in which Mn-dissolution rates of 2.5% for the 1st cycle and 3.5% for the 2nd cycle were reported.¹⁰

The desorption with $(\text{NH}_4)_2\text{S}_2\text{O}_8$ showed significantly lower Mn release than the desorption with HCl . Hydrolysis of $\text{S}_2\text{O}_8^{2-}$ produces $\text{SO}_4^{\cdot-}$ radicals upon peroxy bond breakup. The $\text{SO}_4^{\cdot-}/\text{SO}_4^{2-}$ transformation has a high reduction potential ($E = +2.43$ V) compared to $\text{Mn}^{\text{III}}/\text{Mn}^{\text{II}}$ ($E = +1.54$ V). Accordingly, the affinity of electron uptake for $\text{SO}_4^{\cdot-}$ is higher than that of Mn^{II} . The $\text{SO}_4^{\cdot-}$ radicals replace Mn^{III} as the electron acceptor of the $\text{Li}_x(\text{Mn}_y^{\text{III}}\text{Mn}_z^{\text{IV}})\text{O}_4$ -framework and thus inhibit the reduction of Mn^{III} .¹⁶

The Mn release was much lower when the desorption agent CH_3COOH was used than when using HCl . It also strongly resembled the behavior of $(\text{NH}_4)_2\text{S}_2\text{O}_8$. While HCl belongs to the strong acids, CH_3COOH belongs to the medium acids. The higher pH of the CH_3COOH solution inhibits disproportionation effects described in eqn (6); thus, less water-soluble Mn^{II} is formed.

4.5 Material characterization

The precursor $\text{Li}_{1.6}\text{Mn}_{1.6}\text{O}_4$ was successfully synthesized by hydrothermal synthesis. The samples are indexed as cubic spinel structure of $\text{Li}_{1.6}\text{Mn}_{1.6}\text{O}_4$ with the space group of $Fd\bar{3}m$ which corresponded to ICDD 00-052-1841. Calcining LiMnO_2 a mixture consisting of cubic spinel structure and further Mn-oxide compounds was observed. The spinel structure is preserved following the desorption with HCl as well as with CH_3COOH and $(\text{NH}_4)_2\text{S}_2\text{O}_8$. However, the XRD analyses presented that the intensity of characteristic reflections for all adsorbents treated with desorption agent decreased and formation of new phases, some of which are amorphous, is observed. The decrease in peak intensity was particularly noticeable in the adsorbent regenerated with CH_3COOH . The diffractogram of the adsorbent treated with $(\text{NH}_4)_2\text{S}_2\text{O}_8$ shows reflections between 10° and 15° , which are not seen in the raw adsorbent or in the other adsorbents treated with acid. These newly formed phases are various sulfur compounds formed by the reaction of the desorption agent with the adsorbent.

The SEM images show that treatment, regardless of the type of the used desorption agent, caused changes in the adsorbent morphology. When it is compared with the morphology of the raw adsorbent, the most remarkable morphology change was observed on the adsorbent that is treated with CH_3COOH . This is consistent with the diffraction patterns of the XRD analysis. The morphology of the adsorbent that is treated with HCl shows the greatest similarity to the raw adsorbent in both SEM and XRD analyses.

Although the adsorbent is characterized by a high selectivity towards lithium, the laboratory tests showed a pronounced accumulation of competing ions. This circumstance is due to the high mineralization of the Bruchsal brine of 130 g l^{-1} . While the brine chemistry is dominated by cations such as sodium, potassium, or calcium with twenty to two hundred times higher concentrations, lithium (with an average of 150 mg l^{-1}) represents a trace element in the brine.

The competition of lithium with other alkaline (and earth alkaline) metals for exchanging sites result in the enrichment of competing ions, regardless of the desorption agent used.



However, the analyses of the adsorbent showed that the highest accumulation of lead, barium, calcium, potassium, and iron occurred when CH_3COOH is used. It is remarkable that the accumulation of sodium, calcium and potassium is for all desorption agents comparatively low considering that they are present in high concentrations in the geothermal brine. Nevertheless, the accumulated amounts of these ions are not negligible and can lead to losses of the adsorbent performance. The quantity of iron embedded in the adsorbent is relatively high. This may be caused by precipitation of iron compounds. These precipitates occur after a certain storage time of the geothermal water under atmospheric conditions and are related to temperature and pH change as well as reaction with oxygen after sampling from the geothermal water system. In extraction processes on an industrial scale, which take place under oxygen exclusion and operating conditions, these effects are to be expected to be less significant. The accumulation of competing ions on the one hand can lead to a reduction in the lithium adsorption capacity. On the other hand, naturally occurring radionuclides dissolved in the geothermal brine can also accumulate.

Accumulations of lead ions include also radioactive ^{210}Pb . Furthermore, an accumulation of unstable radium isotopes (especially the long-lived ^{226}Ra) may occur during barium accumulation due to the chemically similar behavior of barium and radium (ionic radii: $\text{Ra}^{2+} = 162 \text{ pm}$; $\text{Ba}^{2+} = 149 \text{ pm}$).²¹ Further importance is attached to ^{40}K , a naturally occurring primordial radioactive isotope of the chemical element potassium.

The extent to which these radioactive isotopes may accumulate on the adsorbent during lithium extraction must be tested by further investigation. So far, no radiochemical analyses are available. Nevertheless, this information is essential for the assessment of radiation exposure. In addition to a qualitative and quantitative evaluation of a potential radionuclide accumulation, the growth characteristics during the adsorption/desorption cycles should also be investigated. The better the physico-chemical processes are understood, the more likely a suitable countermeasure can be developed.

5. Conclusion

The purpose of this research was to investigate the desorption properties of HCl, CH_3COOH and $(\text{NH}_4)_2\text{S}_2\text{O}_8$. Based on the preliminary tests conducted, it can be concluded that achieving high Li^+ recovery and low Mn dissolution during desorption is possible with the use of CH_3COOH and $(\text{NH}_4)_2\text{S}_2\text{O}_8$. Similarly, these desorption agents have been proven by kinetics experiments to have a high reaction rate, which makes them favorable for technical applications. A comparison of the parameters: Li^+ recovery, Mn dissolution, preservation of the crystal structure and accumulation of the competing ions in the ion sieve $\text{H}_{1.6}\text{Mn}_{1.6}\text{O}_4$ using several desorption agents are shown in Table 5.

Table 5 Evaluation of desorption agents in terms of possible use in technical applications: the sign + corresponds to a positive, – to a negative and 0 to a neutral valuation

| | HCl | CH_3COOH | $(\text{NH}_4)_2\text{S}_2\text{O}_8$ |
|-----------------------------|-----|--------------------------|---------------------------------------|
| Li^+ recovery | + | + | 0 |
| Mn dissolution | – | + | + |
| Crystal structure | + | 0 | 0 |
| Accumulation competing ions | 0 | – | 0 |

In the long-term experiments, higher Li^+ adsorption and Li^+ recovery was obtained with the use of HCl and CH_3COOH compared to that using $(\text{NH}_4)_2\text{S}_2\text{O}_8$. Among these desorption agents, HCl caused by far the highest Mn dissolution after eight cycles. Therefore, the decrease of adsorption capacity over cycles is not due to Mn dissolution alone, but also due to competing ion accumulation, which was lowest with HCl. Using $(\text{NH}_4)_2\text{S}_2\text{O}_8$, the decrease in performance is additionally due to the reaction of the adsorbent with the desorption agent, which leads to the formation of new phases. None of the adsorbents caused a severe change on the spinel structure of the treated. However, a remarkable decrease in the intensity of the adsorbent characteristic reflections was observed, especially with the use of CH_3COOH . Also, an accumulation of competing ions occurred on all treated adsorbents, and it was particularly remarkable when CH_3COOH was used. Since radionuclides naturally occur in the deep geothermal water of the Upper Rhine Valley may accumulate on the ion sieve and cause radiation exposure, the accumulation of competing ions is an important parameter in the process.

These results of the laboratory tests are based on only eight adsorption/desorption cycles, which limits the evaluation of long-term performance of desorption agents in terms of Li^+ recovery, Mn dissolution, adsorbent structural change, and accumulation of competing ions. In addition, the tests were performed at a concentration of 0.5 M only, so concentration effects were not considered. Furthermore, the determination accuracy of the reaction rate in the first two minutes of the kinetics experiments was limited by experimental setup.

Further cyclic experiments more than eight cycles can provide additional information about the long-term performance of desorption agents and competing ion accumulation. The latter should also be tested increasing the amount of adsorbent used to determine the radiation load in the ion sieve with high accuracy. To be able to determine the reaction rate in the first two minutes more precisely, it is necessary to minimize the systematic errors and uncertainty in the manual timing during experimental work. Furthermore, it could be tested whether a variation in concentration causes a further optimization in the desorption step. In terms of technical availability, CH_3COOH offers advantages over HCl due to less environmentally hazardous properties, higher occupational safety, and comparable Li^+ recovery. Establishing a Li^+ recovery process based on adsorption technology using CH_3COOH as a desorption agent may enable sustainable Li^+ recovery and help building a domestic lithium supply chain in the future. A transition from laboratory to a pilot



scale will surely represent a challenge. For this, an upscaling of the sorbent production with consistent quality and high chemical stability is crucial. It is also necessary to develop suitable formulations of the adsorbent that provide easy handling in the process but have little impact on the adsorption capacity.

Conflicts of interest

The authors declare that they have no known competing financial interests or personal relationships that could have appeared to influence the work reported in this publication.

Acknowledgements

The authors gratefully acknowledge the reviewing support by C. Patzschke.

References

- 1 Federal Ministry for Economic Affairs and Energy, Renewable energy sources in figures – National and International Development-2019, *BMWI*, 2020.
- 2 J. Vine, *Lithium Resources and Requirements by the Year 2000*, US Government Publishing Office, 1976.
- 3 B. Swain, Recovery and recycling of lithium: A review, *Sep. Purif. Technol.*, 2017, **172**, 388–403.
- 4 P. Greim, *et al.*, Assessment of lithium criticality in the global energy transition and addressing policy gaps in transportation, *Nat. Commun.*, 2020, **11**, 4570.
- 5 S. Zhu, *et al.*, Highly Photoluminescent Carbon Dots for Multicolor Patterning, Sensors, and Bioimaging, *Angew. Chem., Int. Ed.*, 2013, **52**(14), 3953–3957.
- 6 S. Regenspurg, *et al.*, Mineral precipitation during production of geothermal fluid from a Permian Rotliegend reservoir, *Geothermics*, 2015, **54**, 122–135.
- 7 B. Sanjuan, *et al.*, Major geochemical characteristics of geothermal brines from the Upper Rhine Graben granitic basement with constraints on temperature and circulation, *Chem. Geol.*, 2016, **428**, 27–47.
- 8 P. Herzberger, *et al.*, The geothermal power plant Bruchsal, *Geotherm. Energy*, 2010.
- 9 X. Shi, *et al.*, Synthesis and properties of $\text{Li}_{1.6}\text{Mn}_{1.6}\text{O}_4$ and its adsorption application, *Hydrometallurgy*, 2011, **110**(1), 99–106.
- 10 R. Chitrakar, *et al.*, Recovery of Lithium from Seawater Using Manganese Oxide Adsorbent ($\text{H}_{1.6}\text{Mn}_{1.6}\text{O}_4$) Derived from $\text{Li}_{1.6}\text{Mn}_{1.6}\text{O}_4$, *Ind. Eng. Chem. Res.*, 2001, **40**(9), 2054–2058.
- 11 F. Qian, *et al.*, K-gradient doping to stabilize the spinel structure of $\text{Li}_{1.6}\text{Mn}_{1.6}\text{O}_4$ for Li^+ recovery, *Dalton Trans.*, 2020, **49**, 10939–10948.
- 12 L. Aquilina, *et al.*, Water–rock interaction processes in the Triassic sandstone and the granitic basement of the Rhine Graben: geochemical investigation of a geothermal reservoir, *GCA*, 1997, **61**, 4281–4295.
- 13 H. Pauwels, *et al.*, Chemistry and isotopes of deep geothermal saline fluids in the Upper Rhine Graben: Origin of compounds and water–rock interactions, *GCA*, 1993, **57**, 2737–2749.
- 14 H. Mergner, *et al.*, Geothermal Power Generation – First Operation Experiences and Performance Analysis of the Kalina Plant in Bruchsal, *PowerGen*, 2013.
- 15 J. Xiao, *et al.*, Lithium-ion adsorption–desorption properties on spinel $\text{Li}_4\text{Mn}_5\text{O}_{12}$ and pH-dependent ion-exchange model, *Adv. Powder Technol.*, 2015, **26**, 589–594.
- 16 K. Shi, *et al.*, Extraction of Lithium from Single-Crystalline Lithium Manganese Oxide Nanotubes Using Ammonium Peroxodisulfate, *iScience*, 2020, **23**(11), 101768.
- 17 H. M. Leicester and H. S. Klickstein, *A Source Book in Chemistry*, Springer, 1884, vol. 1400–1900, pp. 481–483.
- 18 T. Plenefisch, *et al.*, *Tiefe Geothermie – mögliche Umweltauswirkungen infolge hydraulischer und chemischer Stimulationen*, Umwelt Bundesamt, 2015, ISSN: 1862-4804.
- 19 W. Henry, III, Experiments on the quantity of gases absorbed by water, at different temperatures, and under different pressures, *Philos. Trans. R. Soc.*, 1803, **93**, 29–274.
- 20 A. Gao, *et al.*, The mechanism of manganese dissolution on $\text{Li}_{1.6}\text{Mn}_{1.6}\text{O}_4$ ion sieves with HCl, *Dalton Trans.*, 2018, **47**, 3864–3871.
- 21 R. D. Shannon, Revised effective ionic radii and systematic studies of interatomic distances in halides and chalcogenides, *Acta Crystallogr.*, 1976, **32**, 751–767.

